Received: 23 January 2023 | Revised: 2 August 2023 | Accepted: 23 August 2023

DOI: 10.1002/nbm.5038

RESEARCH ARTICLE

NMR IN BIOMEDICINE WILEY

Improved reliability of perfusion estimation in dynamic susceptibility contrast MRI by using the arterial input function from dynamic contrast enhanced MRI

Chih-Hsien Tseng[1,2,3] | Jaap Jaspers[3,4] | Alejandra Mendez Romero[3,4] | Piotr Wielopolski[5] | Marion Smits[2,5,6] | Matthias J.P. van Osch[2,3,7] | Frans Vos[1,2,3,5]

[1]Department of Imaging Physics, Delft University of Technology, Delft, the Netherlands

[2]Medical Delta, Delft, the Netherlands

[3]Holland Proton Therapy Center Consortium—Erasmus MC, Rotterdam, Holland Proton Therapy Centre, Delft, Leiden University Medical Center, Leiden and Delft University of Technology, Delft, the Netherlands

[4]Department of Radiotherapy, Erasmus MC Cancer Institute, University Medical Center Rotterdam, Rotterdam, the Netherlands

[5]Department of Radiology and Nuclear Medicine, Erasmus MC, University Medical Center Rotterdam, Rotterdam, the Netherlands

[6]Brain Tumour Center, Erasmus MC Cancer Institute, University Medical Center Rotterdam, Rotterdam, the Netherlands

[7]C.J. Gorter MRI Center, Department of Radiology, Leiden University Medical Center, Leiden, the Netherlands

Correspondence
Chih-Hsien Tseng, Department of Imaging Physics, Delft University of Technology, Lorentzweg 1, 2628 CJ Delft, the Netherlands.
Email: c.tseng@tudelft.nl

Funding information
HollandPTC-Varian Consortium; Medical Delta Cancer Diagnostics 3.0

Abstract

The arterial input function (AIF) plays a crucial role in estimating quantitative perfusion properties from dynamic susceptibility contrast (DSC) MRI. An important issue, however, is that measuring the AIF in absolute contrast-agent concentrations is challenging, due to uncertainty in relation to the measured R_2^*-weighted signal, signal depletion at high concentration, and partial-volume effects. A potential solution could be to derive the AIF from separately acquired dynamic contrast enhanced (DCE) MRI data. We aim to compare the AIF determined from DCE MRI with the AIF from DSC MRI, and estimated perfusion coefficients derived from DSC data using a DCE-driven AIF with perfusion coefficients determined using a DSC-based AIF. AIFs were manually selected in branches of the middle cerebral artery (MCA) in both DCE and DSC data in each patient. In addition, a semi-automatic AIF-selection algorithm was applied to the DSC data. The amplitude and full width at half-maximum of the AIFs were compared statistically using the Wilcoxon rank-sum test, applying a 0.05 significance level. Cerebral blood flow (CBF) was derived with different AIF approaches and compared further. The results showed that the AIFs extracted from DSC scans yielded highly variable peaks across arteries within the same patient. The semi-automatic DSC–AIF had significantly narrower width compared with the manual AIFs, and a significantly larger peak than the manual DSC–AIF. Additionally, the DCE-based AIF provided a more stable measurement of relative CBF and absolute CBF values estimated with DCE–AIFs that were compatible with previously reported values. In conclusion, DCE-based AIFs were reproduced significantly better across vessels, showed more realistic profiles, and delivered more stable and reasonable CBF measurements. The DCE–AIF can, therefore, be considered as an alternative AIF source for quantitative perfusion estimations in DSC MRI.

Abbreviations: aCBF, absolute cerebral blood flow; AIF, arterial input function; CBF, cerebral blood flow; CBV, cerebral blood volume; CV, coefficient of variation; DCE, dynamic contrast enhanced; DSC, dynamic susceptibility contrast; FOV, field of view; FWHM, full width at half-maximum; GM, grey matter; IDH, isocitrate dehydrogenase; MCA, middle cerebral artery; MTT, mean transition time; rCBF, relative cerebral blood flow; RIGEL, Radiotherapy in Isocitrate dehydrogenase mutated Glioma: Evaluation of Late outcomes; ROI, region of interest; SPGR, spoiled gradient-recalled; WM, white matter.

KEYWORDS
arterial input function, cerebral blood flow, cerebral blood volume, dynamic contrast enhanced MRI, dynamic susceptibility contrast MRI

1 | INTRODUCTION

Over the past three decades, dynamic susceptibility contrast (DSC) MRI has emerged as a powerful tool for studying the brain's haemodynamic characteristics. It is applied to estimate perfusion properties in patients with various pathologies, including stroke and cancer patients: for example, the cerebral blood volume (CBV), cerebral blood flow (CBF), and mean transition time (MTT).[1,2] Additionally, timing parameters, such as time-to-bolus-peak, were found to have important clinical value.[3] The estimation of tissue perfusion properties is based on indicator dilution theory[4] and is driven by the measurement of the arterial input function (AIF). The AIF represents the time-varying contrast-agent concentration measured in arterial blood supplying the tissue under investigation. Ideally, it should be measured directly in the artery supplying the tissue of interest. However, in practice it is usually derived from a large artery, such as the internal carotid artery or middle cerebral artery (MCA).

An issue in estimating the perfusion properties is that the relation between the ΔR_2^*-weighted DSC signal and the contrast-agent concentration is uncertain. For practical reasons it is often assumed that contrast-induced changes in R_2^* are linearly proportional to the contrast-agent concentration. However, some studies showed that the relation is rather more quadratic than linear, as well as dependent on the haematocrit level in blood.[5–8] Moreover, three effects can affect the shape of the measured AIF severely. First, the AIF is assumed to be measured in pure blood, which will never be the case, as limited spatial resolution leads to mixing of structures, known as partial-volume effects.[9] Such partial-volume effects can lead to highly nonlinear distortions of the measured AIF. Second, the signal in large arteries tends to reach the noise floor during the passage of contrast agents, leading to signal depletion.[10] This is due to the commonly applied choice of a single, long echo time in clinical practice, which is optimal for capturing the bolus passage in brain tissue. Third, the time–concentration curve from voxels inside an artery, especially the peak, can become distorted due to displacement effects resulting from the increase of the local precession frequency induced by the paramagnetic contrast agent within the artery.[11]

Dynamic contrast enhanced (DCE) MRI is another perfusion technique enabling estimation of cerebral haemodynamics, which is based on the R_1 effects induced by the contrast agent. Importantly, the relation between the R_1 relaxation rate and contrast concentration in blood has been studied comprehensively and is more stable under different conditions than R_2^*-based measurements.[12] As such, DCE imaging holds the potential to provide a more accurate AIF measurement in absolute units (i.e., in mM). Furthermore, the spoiled gradient-recalled (SPGR) imaging sequence that is commonly used for DCE MRI provides somewhat higher spatial resolution, reducing partial-volume effects. Still there are two issues when measuring the AIF with DCE MRI. First, fresh, unsaturated protons can flow into the imaging volume, while they are assumed to be saturated, leading to underestimation of the contrast-agent concentration: this is referred to as the inflow effect.[13,14] Lately, however, several approaches were proposed to ameliorate the inflow effect.[15–17] Second, concomitant T_2^* effects induced by high contrast concentration may confound the measured R_1-weighted signal enhancement.[18] This effect can be diminished by using a sufficiently short echo time for the DCE sequence.

We hypothesized that a DCE-based AIF measurement might improve perfusion measurement in DSC MRI compared with using a DSC-based AIF measurement. Of course, the need for two contrast-agent based MRI scans might make such an approach clinically impractical at first sight. However, a preload contrast injection is frequently applied in DSC MRI in order to saturate the extravascular space to minimise errors by contrast-agent leakage.[19,20] Therefore, this preloading stage might be exploited by performing DCE image acquisition, from which a potentially improved AIF could be obtained. In addition to AIF determination, these data could also be used for leakage quantification and estimating vascular permeability, but this is not the focus of the current study.

In this study, we aimed to compare the AIFs measured from DCE and DSC MRI, as well as the effect of the different AIF approaches on the estimation of perfusion properties. To do so, we performed combined DCE and DSC imaging in patients suffering from diffuse gliomas as included in an ongoing study into effects of radiotherapy. The characteristics of the AIFs from both DCE and DSC imaging were studied systematically. Furthermore, perfusion parameters were compared when using the two different AIFs.

2 | METHODS

2.1 | Patient cohort

Data in this study were acquired as part of an associated clinical study in the Netherlands: the Radiotherapy in isocitrate dehydrogenase (IDH) mutated Glioma: Evaluation of Late outcomes (RIGEL) study (trial identifier: NCT04304300). The first 10 patients who had histologically

TABLE 1 Patient cohort.

Patient number	Age	Sex		Tumor hemisphere		MRI timing	
$N = 10$	36.1± 10.3	Male	7	Right	8	Pre-treatment	7
		Female	3	Left	2	Post-treatment	2
						Both	1

confirmed, IDH mutated glioma (WHO grade 2 or 3) and for whom the relevant imaging data were available were included in this substudy. Informed consent was obtained from all individual participants. Postoperative radiation therapy and chemotherapy were given to every patient after surgical tumor resection. MRI was performed before and approximately 4 months after radiation therapy. From one patient, DSC and DCE images were obtained before and after radiation therapy, from two patients scans were only made post-treatment, and from seven patients the pre-treatment images were included. Table 1 collates the relevant information for our patient cohort.

2.2 | Imaging and injection protocol

Imaging was performed on a 3T MRI system (Signa Premier, GE Healthcare, Wisconsin, USA) with a 48-channel head coil in the Erasmus MC (Rotterdam, the Netherlands).

Prior to contrast-enhanced imaging, a high resolution T_1-weighted image was acquired using an inversion recovery preparation, 3D fast spoiled gradient echo sequence (brain volume imaging, BRAVO) with TR/TE: 7.6/3.1 ms, inversion time: 450 ms, flip angle: 12°; field of view (FOV): 240 × 240 × 175 mm^3, matrix size: 256 × 256 × 176, in-plane resolution: 0.94 × 0.94 mm^2.

In each patient, 7.5 ml of Gadobutrol (Gadovist®, Bayer, Germany), corresponding to a standard dose for a 75-kg patient, followed by a 15-mL saline flush were automatically injected with a 22-g cannula via the antecubital vein at 5 $mL \cdot s^{-1}$ by a power injector (Spectris Solaris EP, MEDRAD, Pennsylvania, USA), during which DCE imaging was performed. Immediately after DCE acquisition, a second bolus of contrast agents with the same dose and protocol was injected, during which DSC imaging was done. The contrast-agent injections were started 20 seconds after commencing the DCE and DSC acquisitions.

DCE images were acquired using a differential subsampling with Cartesian ordering (DISCO) sequence[21] with TR/TE: 2.7/0.9 ms, flip angle: 14°; FOV: 220 × 220 × 142 mm^3, matrix size: 128 × 128, 72 slices, in-plane resolution: 1.7 × 1.7 mm^2, slice thickness: 2 mm, temporal resolution: 2 s, yielding 183 dynamics at a total scan time of 6 minutes and 20 seconds. DSC images were obtained with a T_2^*-weighted gradient-echo echo-planar imaging sequence with TR/TE: 2000/45 ms, FOV: 220 × 220 × 140 mm^3, matrix size: 100 × 100, 29 slices, in-plane resolution: 2.2 × 2.2 mm^2, slice thickness: 5 mm, temporal resolution: 2 s, yielding 50 dynamics in total.

2.3 | Preprocessing

All image processing was done with in-house created software in MATLAB R2020a (The MathWorks, Inc., Natick, Massachusetts, United States). Head motion between the dynamic scans (both DCE and DSC images) was checked visually by monitoring the three cross-sectional lines of central coronal, sagittal, and axial slices across time. In cases in which misalignment of the boundaries in these orthogonal slices was observed, this was corrected by performing image registration of the entire series to the first volume. Registration was done by a 3D rigid transformation optimizing the normalized mutual information as implemented in SPM12.[22] Subsequently all DSC volumes were resampled to 72 slices and registered to the first DCE volume with the same registration approach. Finally, all volumes were resampled to share the same image coordinates and voxel size.

2.4 | AIF selection

AIF measurements were obtained in three ways. From the DCE data, the DCE–AIF was determined via manual selection based on the criteria described below. From the DSC data, AIFs were obtained by two different approaches: (1) projection of the manually selected voxels from the DCE images onto the DSC images followed by a manual correction step (see below); (2) a semi-automatic identification from the DSC series. The latter two AIFs will be referred to as the *manual DSC–AIF* and the *semi-automatic DSC–AIF*, respectively.

2.4.1 | DCE–AIF measurement

In every dataset, five different arteries belonging to the territory of the MCA were identified visually based on clearly observable signal changes during the upslope of the contrast-agent passage. In each such artery, a group of voxels were delineated inside the artery. Such regions of interest (ROIs) were placed in the central part of vessels to limit partial-volume effects as much as feasible. Subsequently, the selected ROIs were projected onto the entire DCE time series. The resulting concentration–time curves were not reviewed based on visual quality in any way.

2.4.2 | DSC–AIF measurement

First, the selected voxels of the five arteries in the DCE images were copied onto all the registered DSC images. These copied ROIs could subsequently be adjusted slightly to make sure that they were all located inside the artery. This step was added to compensate for small misregistrations when deemed necessary. The resulting ROI was then projected on the entire DSC series. Again, the resulting concentration–time curves were not reviewed for visual quality.

Secondly, a semi-automatic technique for AIF selection was applied based on a clustering approach favoring early bolus arrival time, large area under curve, and small residual error of a fit with a gamma function.[23] Initial experiments were performed first to optimize the search region and the optimal number of selected voxels by the algorithm. The tuning procedure is illustrated in the supplementary material (Figure S1). Subsequently, the optimal settings were applied in the same five slices of the DCE–AIF determination. In each slice, the algorithm automatically identified a group of voxels in which the signal resembled an AIF, irrespective whether they resided inside an artery. No further corrections were applied to the selected voxels.

The signals in each ROI (manual selection) and group of voxels (semi-automatic selection) were averaged to yield mean time–intensity curves. Thus, for each type of AIF (DCE–AIF, manual DSC–AIF, semi-automatic DSC–AIF), five such curves were generated for each patient. The mean time–intensity curves were subsequently normalised by dividing them by the average signal of the first five time points (i.e., baseline points) to produce signal ratio curves, which were used to derive contrast concentration–time curves. Figure 1 summarizes our AIF selection procedure.

2.5 | AIF calculation from DCE images

A previously published approach[17] was applied to compensate for potential underestimation of contrast concentration due to inflow effects. Specifically, a parameterized version of Orton's AIF model,[24] constrained by a fixed area under the first passage reflecting the known injection dose, was first fitted to the DCE signal ratio curve to estimate the number of excitation pulses experienced by the protons. Subsequently, the estimated number of pulses was used to calculate the contrast-agent concentration at each time point so that the underestimation from the inflow effect was corrected for. The inflow-compensated signal ratio curves from the DCE images were transformed into contrast concentration–time curves by assuming a linear relation between the concentration and the T_1 relaxivity[25]; the longitudinal relaxivity in plasma (asserting a haematocrit level of 0.45) at 3.0T was assumed to be 4.5 $\mathrm{L}\cdot(\mathrm{mM}\cdot\mathrm{s})^{-1}$ for gadobutrol at 37 °C,[12] and the initial T_1 value of blood was set to 1.6 s.[26]

2.6 | AIF calculation from DSC images

The DSC-driven AIFs were first translated into concentration–time curves by the most commonly used conversion model. As such, ΔR_2^* was assumed to be linearly related to the contrast-agent concentration. We initially computed

$$\Delta R_2^*(t) = \frac{-1}{TE}\cdot \ln Sr(t), \tag{1}$$

in which TE is the echo time of the DSC sequence and $Sr(t)$ is the signal ratio curve (see Section 2.4). Subsequently, relying on the linearity assumption, we determined the contrast-agent concentration by applying a proportionality constant of 16.5 $(\mathrm{mM}\cdot\mathrm{s})^{-1}$, which we derived from the linear approximation of a quadratic model at contrast concentrations ranging from 0–10 mM.[8] Dividing ΔR_2^* by this constant yielded the contrast concentration for the manual and semi-automatic DSC–AIFs.

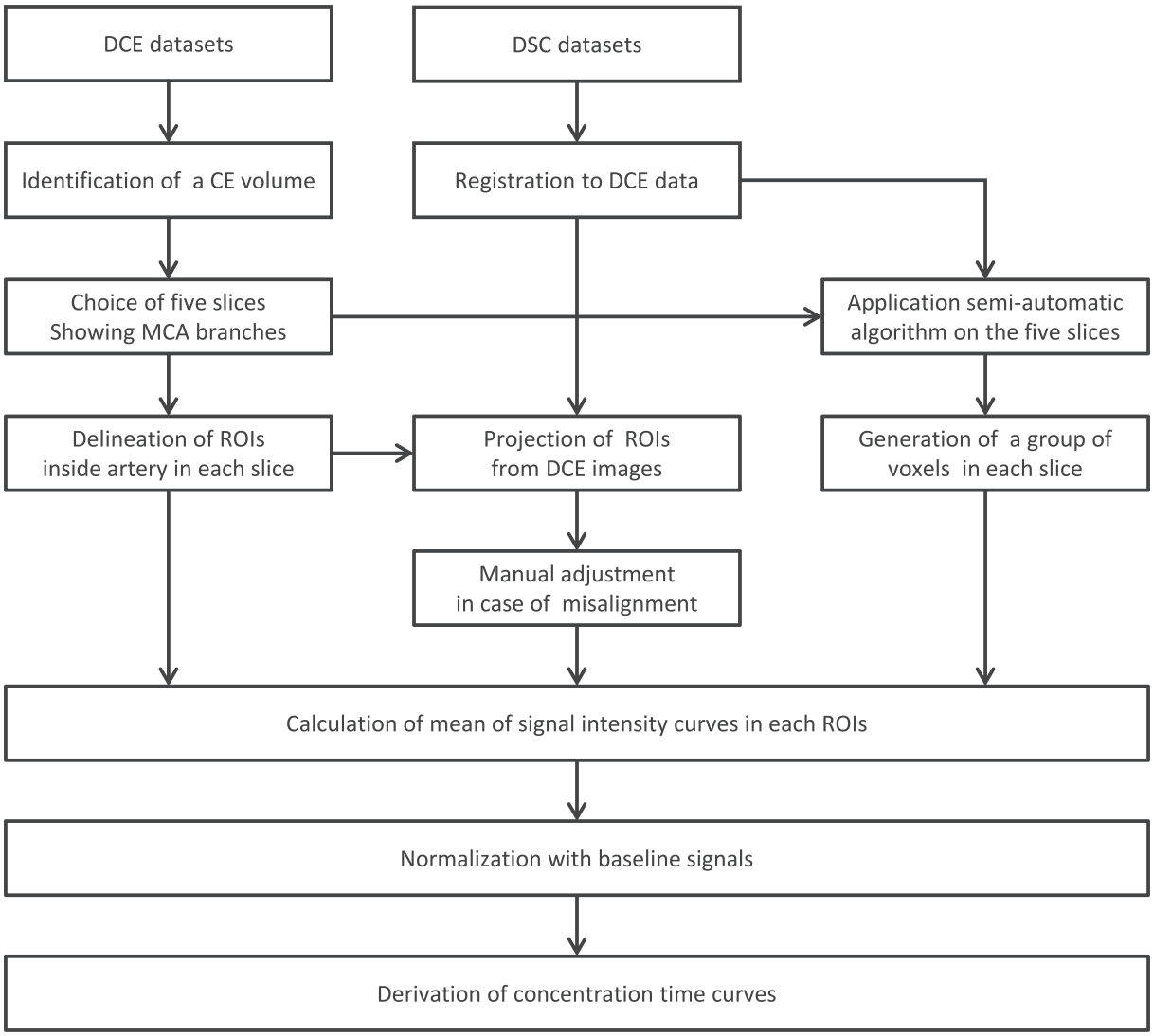

FIGURE 1 Flowchart of our AIF selection procedure. Abbreviations: CE, contrast enhanced; MCA, middle cerebral artery; ROI, region of interest.

2.7 | Quantitative assessment of AIF curves

For each method in every patient, the mean and variance of the peak values and the full widths at half-maximum (FWHMs) of the AIFs were determined and compared between the methods. Differences were statistically assessed using the Wilcoxon rank-sum test. *P*-values smaller than 0.05 were considered as statistically significant. Scatter plots and Bland–Altman plots were created for comparison of differences between methods.

2.8 | Perfusion coefficients

CBF was calculated from the DSC data based on a conventional tracer kinetic model,[27] in which the relationship between the tissue response and the AIF is defined through a convolution integral:

$$\frac{1-Hct_{LV}}{\rho\cdot(1-Hct_{SV})}\cdot C_t(t)=CBF\cdot(C_a(t)*R(t)), \tag{2}$$

in which ρ is the assumed density of brain tissue, set to 1.04 g· ml^{-1} and Hct_{LV} and Hct_{SV} are the presumed hematocrit levels in large and small vessels of 0.45 and 0.25, respectively, as used in Rempp et al.,[28] $C_t(t)$ is the time–concentration curve in tissue, $C_a(t)$ is the AIF, and $R(t)$ is the

tissue residue function. The latter function describes the fraction of a hypothetical instantaneous bolus of tracer that is still present in the tissue at time t and is obtained by deconvolving $C_t(t)$ with $C_a(t)$. The maximum value of the deconvolution outcome represents the CBF value in the voxel concerned. The block-circulant deconvolution method was applied for this calculation, which has been proven to be less sensitive to delay effects between AIF and tissue-passage curves.[29]

The relative CBF (rCBF) was used to compare the stability and reliability of the various AIF types in perfusion estimation. A group of voxels was manually selected in normal-appearing white matter in a region contralaterally with respect to the tumor location. The rCBF map was produced by dividing all CBF values by the mean of the selected region. The coefficient of variation (CV) in rCBF was computed using the three AIFs measured across the different slices (i.e., rCBF maps were calculated based on the AIFs determined from the five different arteries). The CV in each voxel was then derived by calculating the ratio of the standard deviation and the mean.

In addition, the means of the AIFs in each source were used to estimate an absolute (i.e., quantitative) CBF measure (aCBF). As such, tissue concentration maps were generated by normalizing ΔR_2^* (t) with a previously reported relaxivity value R_2^* in tissue:

$$C(t) = \frac{\Delta R_2^*}{r_2^*}, \tag{3}$$

in which r_2^* was set equal to 85 $(\mathrm{mM \cdot s})^{-1}$.[30] Subsequently, aCBF maps were produced by deconvolving the tissue concentration–time curves with the mean AIFs. This aCBF was registered to the T_1-weighted image via SPM12 for further processing. Tissue probability maps were derived by applying the SPM12 segmentation function on the T_1-weighted image. The hemisphere from which the tumor was removed was masked in each patient. Finally, aCBF values of the remaining, normal appearing grey matter (GM) and white matter (WM) were sampled and compared with values reported in literature.

3 | RESULTS

3.1 | Example DCE and DSC–AIFs

One representative example of AIF selection is shown in Figure 2. The selected region was determined based on the DCE image containing the MCA (Figure 2A) and projected onto the registered, corresponding DSC slice (Figure 2B). Observe that the DCE–AIFs across voxels appear much more consistent and exhibit less variation in peak height than the DSC–AIFs (Figure 2D). The selected arterial-like voxels from the semi-automatic algorithm applied on the same slice are shown in Figure 2C and the AIF calculations from every individually selected voxel are plotted in Figure 2E. Figure 2F shows the characteristics of the AIFs obtained from the three approaches. While the peaks of the two manual approaches are overlapping, the shapes of the DCE–AIF and the manual DSC–AIF appear very similar, especially during the first passage of the contrast bolus. Instead, the semi-automatic DSC–AIF demonstrated higher peak values in combination with a more narrow width compared with the manual DSC–AIF. Further results related to the optimization of the semi-automatic DSC–AIF estimation are included as supplementary material.

The DCE and DSC–AIFs derived from different vessels (or slices) are plotted in Figure 3. Overall, the DCE-based AIFs exhibited better reproducibility visually than the DSC-based AIFs in all patients. Only two patients are shown for illustration purposes, one with relatively small variation of the DSC–AIF peak heights (Figure 3B,C) and one with larger variation in both the peak height and tail shape (Figure 3E,F), which is more representative for the other patients.

3.2 | Quantitative analysis

The mean and the standard deviation of the peak value and FWHM from the AIFs are summarized in Table 2. The CV of the peak values from all DSC–AIFs were larger than those of the DCE–AIFs. The peak value of the DCE–AIF was significantly higher than the peak value of the manual DSC–AIF (p-value: 0.00008). The peak value of the semi-automatic DSC–AIF was significantly higher than the peak values of the DCE–AIF (p-value: 0.03) and manual DSC–AIF (p-value: 0.00008). There was no significant difference between the mean FWHM of the DCE–AIF and the mean FWHM of the manual DSC–AIF. The mean FWHM of the DCE–AIF was significantly larger than the mean FWHM of the semi-automatic DSC–AIF (p-value: 0.0004). Likewise the FWHM of the manual DSC–AIF was significantly larger than the FWHM of the semi-automatic DSC–AIF (p-value: 0.0008). Scatter plots and Bland–Altman plots for comparison of the FWHM values are shown in Figure 4. The mean FWHM difference between the DCE–AIF and the manual DSC–AIF was 0.5 ± 1.6 s (CI (95%) $= [-2.5, 3.6]$). The mean FWHM difference between the DCE–AIF and the semi-automatic DSC–AIF was 3.2 ± 1.6 s (CI (95%) $= [0.1, 6.3]$). Finally, the mean FWHM difference between the two DSC–AIF methods was 2.7 ± 1.2 s (CI (95%) $= [0.3, 5.1]$).

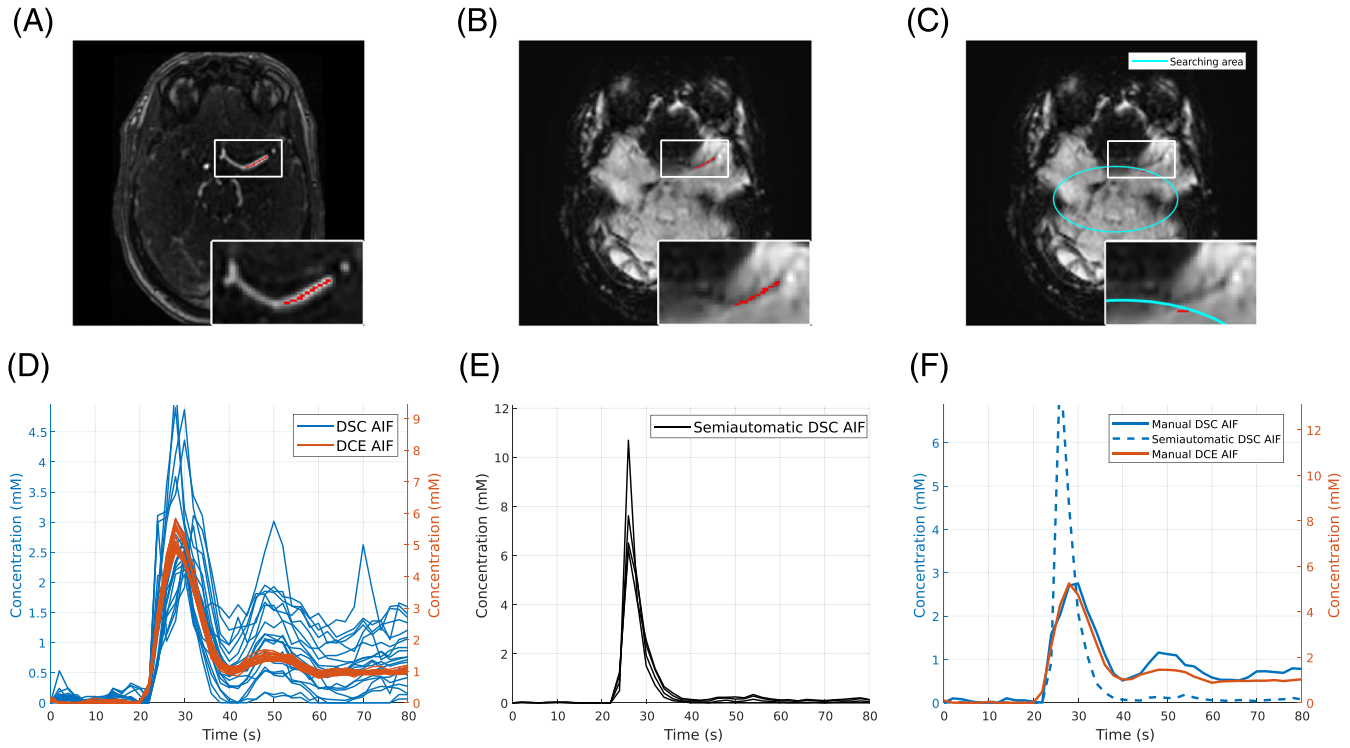

FIGURE 2 Illustration of AIF measurements in a single artery of an example patient. The ROI for calculating the AIF curves was (A) manually selected in the DCE images and (B) subsequently projected onto the registered DSC images. (C) A semi-automatic detection algorithm was applied to the same plane, using default settings; detected voxels are indicated in red. Contrast concentration changes measured in the DCE and DSC series in the voxels from the selected regions in (A) and (B) are plotted in (D). Blue lines are measurements from DSC MRI (left *y*-axis); red lines represent measurements from DCE MRI (right *y*-axis). AIF curves from the automatically detected DSC voxels (C) are shown in (E). The mean DCE–AIF and the two mean DSC–AIFs are compared in (F). The peak of the DCE–AIF was aligned with the peak of the manual DSC–AIF to demonstrate the highly correlated shape of these two AIFs. In comparison, the semi-automatic DSC–AIF showed a sharper and narrower peak than the manual AIFs.

3.3 | CBF analysis

The CV map of the rCBF with different types of AIFs in a representative patient is shown in Figure 5. The mean CVs of whole brain rCBFs calculated with the different AIFs in every patient are listed in Table 3. One can observe that the DCE–AIF provided a more stable rCBF measurement, that is, showing smaller relative variance than the DSC–AIFs did. Means and standard deviations of the sampled aCBF values in the GM and WM masks across individuals are collated in Table 4. The average aCBFs in GM and WM over all patients were 51.5 and 24.0 ml·(100 g)$^{-1}$·min^{-1} with the DCE–AIFs, 110.0 and 44.2 ml·(100 g)$^{-1}$·min^{-1} with the manual DSC–AIFs, and 72.5 and 28.4 ml·(100 g)$^{-1}$·min^{-1} with the semi-automatic DSC–AIFs, respectively. Patient 6 was excluded from the calculation of the group average because severe ringing artefacts were observed (Figure S2). Additional results related to CBV estimation are presented in the supplementary material.

4 | DISCUSSION

This article studied the potential of replacing an AIF from DSC imaging with an AIF from DCE to improve the precision of estimating DSC-based perfusion properties. The DCE-driven AIF showed much more stable peak estimation and smoother curves compared with the DSC–AIFs. In effect, less variation in calculated perfusion parameters could be expected, which was confirmed by the reduced rCBF variance.

We attribute the better reproducibility of the DCE-driven AIF to the absence of detrimental effects, such as susceptibility artefacts, large partial-volume effects, signal depletion, and voxel displacement, which do affect the DSC data. Some previous studies introduced an additional slice or sequence targeting the AIF measurement specifically, to be succeeded by a more comprehensive DSC series.[31–33] Instead of doing this, we exploited the preload injection to perform DCE MRI. As such, it facilitated acquisition of a quantitative AIF, that is, representing contrast-agent concentration instead of change in R_2^* over time.

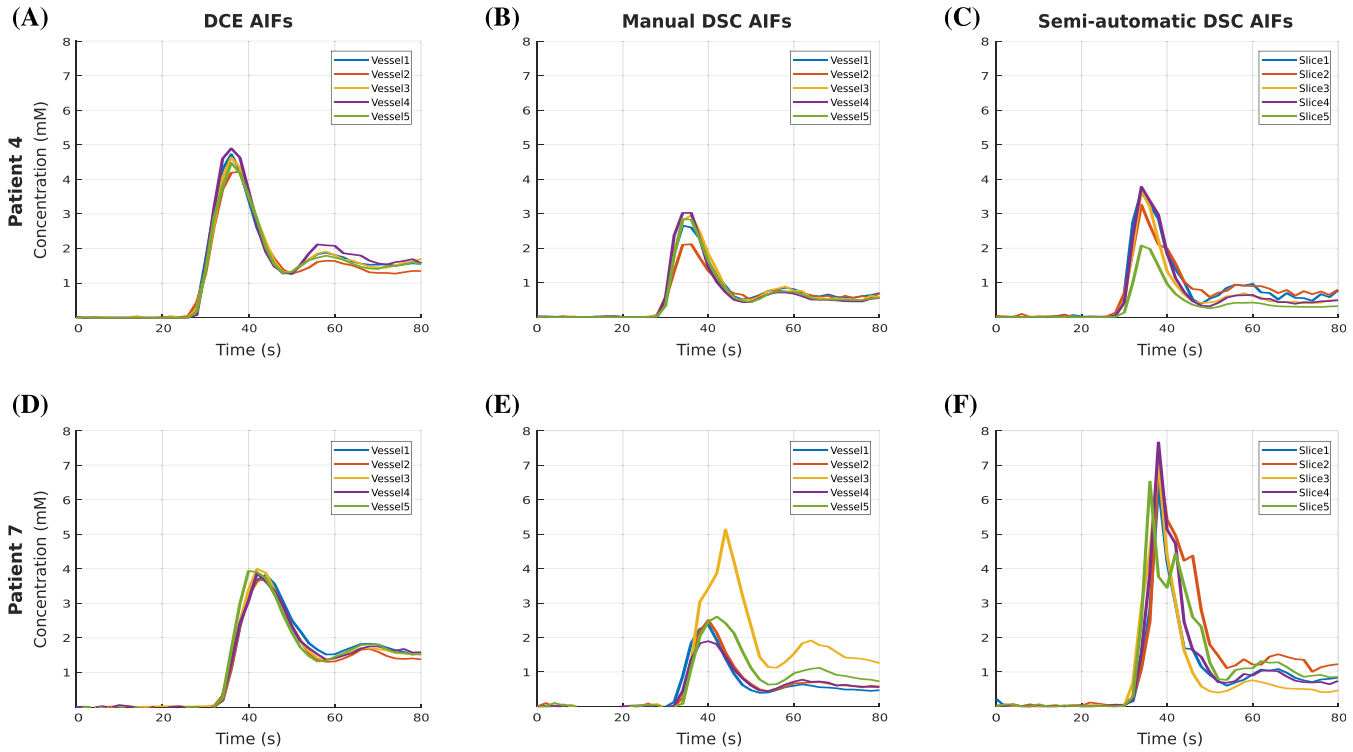

FIGURE 3 AIFs measured in five arteries (see legend) in two representative patients (top and bottom) using three approaches. The DCE-driven AIFs (A, D) indeed show less variation than both the manual (B, E) and semi-automatic (C, F) DSC–AIFs.

TABLE 2 Mean peak values and FWHM and corresponding standard deviations for the different patients and AIF measurement methods.

	DCE–AIF		Manual DSC–AIF		Semi-automatic DSC–AIF	
	Amplitude (mM)	FWHM (s)	Amplitude (mM)	FWHM (s)	Amplitude (mM)	FWHM (s)
Patient 1	9.4±1.1	6.5±0.7	2.5±0.7	5.9±1.2	7.4±2.1	4.6±1.1
Patient 2	5.3±0.3	7.8±0.4	2.8±1.0	10.3±1.4	7.4±1.7	5.7±2.1
Patient 3	6.4±0.3	6.7±0.4	2.6±0.1	6.8±1.9	5.2±1.3	3.9±0.5
Patient 3†	5.7±0.5	8.9±1.6	2.7±0.6	8.5±1.4	5.8±1.5	5.7±1.9
Patient 4†	4.6±0.3	9.0±0.3	2.8±0.4	9.0±0.6	3.4±0.7	7.4±0.8
Patient 5	4.4±0.4	10.5±3.1	2.6±0.7	10.1±1.3	6.0±1.9	6.1±1.1
Patient 6	4.5±0.5	9.4±2.2	2.5±0.7	8.4±0.9	3.8±0.4	6.8±0.3
Patient 7†	4.0±0.1	10.3±0.5	2.9±1.3	10.1±1.4	7.0±0.6	5.6±0.9
Patient 8	4.6±0.5	13.0±2.1	3.0±0.7	8.8±1.7	6.8±1.5	6.0±2.7
Patient 9	5.5±0.7	10.1±2.0	3.0±0.7	9.6±0.8	6.8±1.4	7.6±2.3
Patient 10	6.7±0.3	8.9±0.8	2.6±0.7	7.9±1.5	5.1±1.9	6.3±2.8
Average	5.6±1.7	9.2±1.9	2.7±0.2	8.7±1.4	5.9±1.4	6.0±1.1

Note: Data are reported as mean ± standard deviation.
†Patient received radiation therapy.

There is no agreement in the literature on a standardized approach to measure the AIF for perfusion estimation in DSC MRI, due to several controversies.[34] Specifically, the AIF has been measured in arteries and veins, globally and locally, inside and outside arteries, individually and population-based, and manually or automatically. All these approaches were aimed at minimizing partial-volume effects, signal depletion, AIF dispersion, or any other confounding effects on the measured AIFs. Eventually, the chosen approach will be a compromise of these detrimental effects. Several semi-automatic and automatic measurement methods were proposed to avoid operational bias and simplify the procedure.[23,35–37] Some of these approaches are widely available in commercial software. We used an open-source semi-automatic DSC–AIF algorithm, which detects the arterial voxels using a clustering algorithm with criteria as described by other researchers: early bolus arrival, large

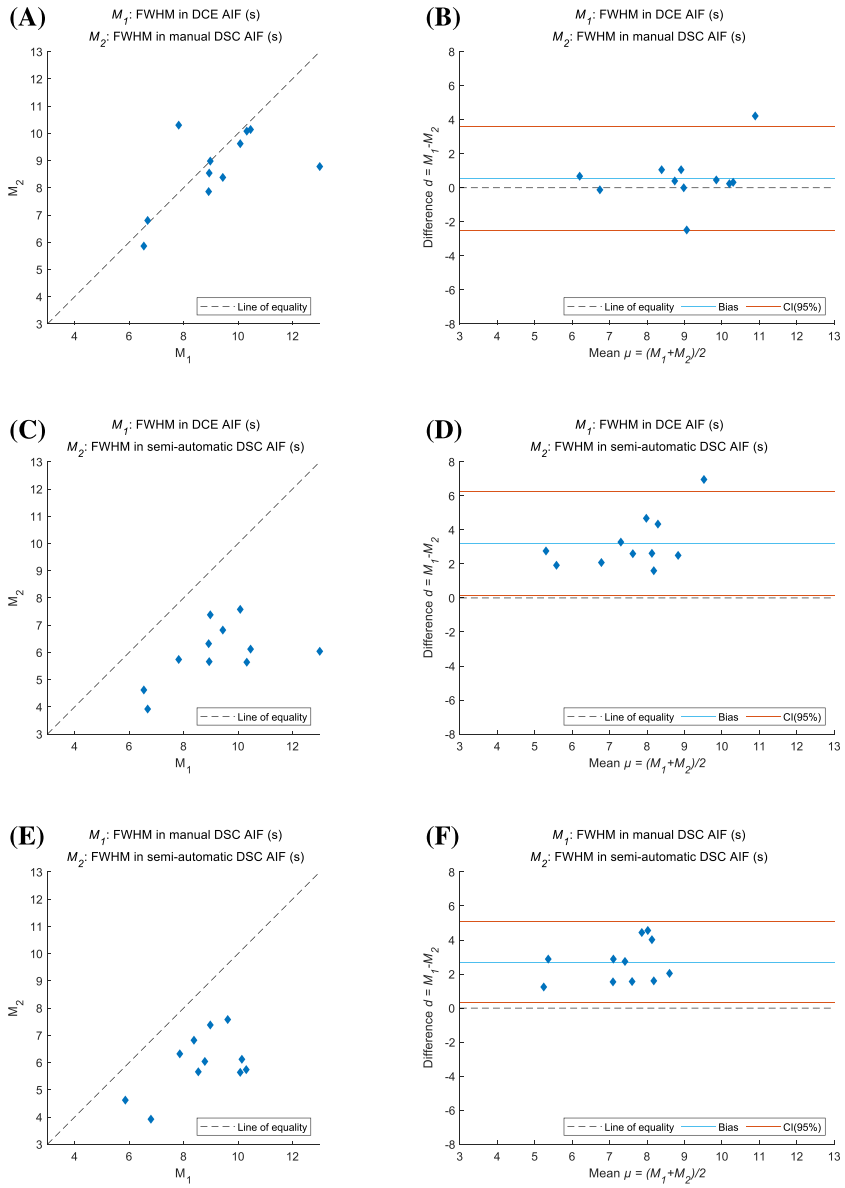

FIGURE 4 (A, C, E) Scatter plot and (B, D, F) Bland–Altman plot of FWHMs calculated from the DCE–AIF, the manual DSC–AIF, and the semi-automatic DSC–AIF.

area under curve, and good fitting with a gamma variate function. However, the resulting AIFs had a higher peak with a narrower width in comparison with the manual AIFs. This probably resulted from the algorithm favoring a larger area under the curve, as this might minimize partial-volume effect. However, van Osch et al[9] suggested that the partial-volume effect may not only induce underestimation of the AIF peak, but also lead to overestimation.

Previously, You et al. concluded that DCE-based pharmacokinetic parameters derived using a DSC–AIF yielded better diagnostic accuracy and reliability for differentiating high-grade astrocytoma from low-grade astrocytoma than those derived with a DCE–AIF,[38] that is, the opposite to this study. Another study from the same group yielded a similar conclusion that the DSC–AIF helped differentiation of glioblastoma from primary central nervous system lymphoma compared with the DCE–AIF.[39] However, in these studies there was a mismatch in temporal resolution of the DCE and DSC acquisition, of 4 and 1.6 seconds, respectively. Furthermore, there was no correction for inflow effects performed on the DCE–AIF measurement, which could cause underestimation of the peak concentration. Indeed, in a later study from the group,[40] the temporal resolution was proven to be the key factor for obtaining high-quality DCE–AIF measurements and yielding better reproducibility of DCE parameters.

Most commonly a linear relation is assumed between the transverse relaxation change and the contrast concentration when deriving the DSC–AIF, as we did in this study. However, others argued that the relationship between the contrast concentration and the signal change in blood

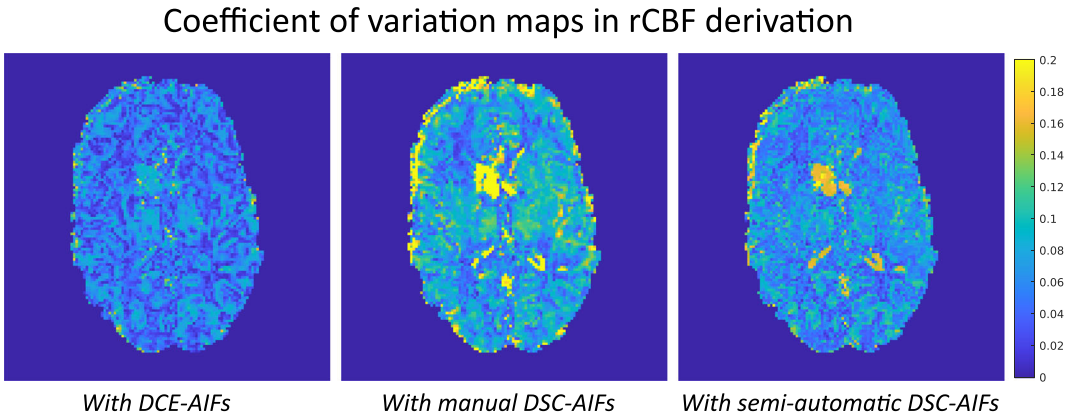

FIGURE 5 Representative coefficient of variation (CV) map (for a single patient) derived from rCBF values computed from the DSC series using (left) the DCE–AIFs, (middle) the manual DSC–AIFs, and (right) the semi-automatic DSC–AIFs. Observe that the DSC–AIFs introduced larger relative variation than did the DCE–AIF.

TABLE 3 Mean coefficient of variation (CV) of rCBFs in whole brain for the different patients and AIF measurement methods.

	Mean CV of rCBF		
	DCE–AIF	Manual DSC–AIF	Semi-automatic DSC–AIF
Patient 1	0.043	0.059	0.063
Patient 2	0.028	0.038	0.083
Patient 3	0.048	0.128	0.073
Patient 3†	0.046	0.056	0.062
Patient 4†	0.026	0.035	0.038
Patient 5	0.025	0.035	0.055
Patient 6	0.024	0.032	0.046
Patient 7†	0.025	0.032	0.044
Patient 8	0.039	0.051	0.085
Patient 9	0.020	0.028	0.052
Patient 10	0.039	0.064	0.072
Average	0.033	0.051	0.061

†Patient received radiation therapy.

is modeled better by a quadratic expression, albeit dependent on the hematocrit level.[5–8] In practice, however, the hematocrit level is not always known. Furthermore, this will vary across the vasculature: for example, there will be a higher hematocrit level in the smallest vessels. Also, the "arterial" voxels often combine both blood and tissue signals with unknown proportion, which increases the linearity of the relation between contrast concentration and signal changes.[7] These issues complicate the application of the quadratic model. In order to calculate aCBF based on DSC–AIFs, we used an assumed proportionality (R_2^*) for DSC–AIFs derived by a linear approximation of the quadratic model which was adjusted for hematocrit level[8]: $16.5\,(\mathrm{mM}\cdot\mathrm{s})^{-1}$. Alternatively, it was theoretically assumed to be $5.9\,(\mathrm{mM}\cdot\mathrm{s})^{-1}$ by Calamante et al[41] and Pedersen et al.[42] Lind and her colleagues derived a linear constant equal to $89\,(\mathrm{mM}\cdot\mathrm{s})^{-1}$ by combining quantitative susceptibility mapping with DSC measurements.[43] Furthermore, Knutsson proposed an approximated value of $20\,(\mathrm{mM}\cdot\mathrm{s})^{-1}$ by linear fitting of the quadratic model (with contrast concentration from 0–10 mM).[44] These figures signify that there is no consensus regarding an optimal R_2^* constant for quantifying AIF in DSC MRI. By applying the AIF derived from the DCE images, we could bypass such quantification issues.

The smaller variation in rCBF estimates using the DCE–AIFs in our opinion reflects that this approach is more reliable and consistent than when using the DSC–AIFs. In practice, only one vessel (or slice) is chosen as the AIF source. Therefore, location independence of the AIF is preferred for optimal consistency and to yield reduced operation bias in perfusion imaging. The average aCBFs estimated with DCE–AIFs in healthy GM and WM were 51.5±7.8 and 24.3±3.9 (unit: $\mathrm{ml}\cdot(100\,\mathrm{g})^{-1}\cdot\mathrm{min}^{-1}$), respectively. These are close to the CBF values obtained by previous MRI,[44–48] CT,[49] and PET[50–52] studies. The average aCBF obtained with the DSC–AIFs was larger than most reported ranges, for GM as well as

TABLE 4 Mean aCBF and corresponding standard deviation in each patient and the average over all patients.

	Absolute CBF (mL·(100 g)$^{-1}$·min^{-1})					
	DCE–AIF		Manual DSC–AIF		Semi-automatic DSC–AIF	
	GM	WM	GM	WM	GM	WM
Patient 1	45.3±20.3	20.4±10.7	149.8±60.7	68.7±35.0	79.1±35.4	35.2±18.9
Patient 2	60.8±28.7	21.9±11.8	92.2±44.0	33.3±17.8	63.8±31.1	22.8±12.9
Patient 3	54.9±24.2	21.4±11.0	154.0±60.1	61.0±30.6	98.8±42.3	37.4±19.7
Patient 3†	44.0±20.5	16.1±8.3	89.9±41.3	33.2±17.2	63.9±30.0	23.1±12.2
Patient 4†	53.7±25.6	20.5±10.1	98.9±46.8	37.8±18.6	96.0±45.7	36.9±17.6
Patient 5	51.4±25.1	19.4±11.0	85.0±41.1	32.1±18.3	59.3±29.3	21.7±13.0
Patient 6	109.4±58.6	58.6±35.7	190.9±82.8	72.3±56.0	152.3±77.1	53.9±43.3
Patient 7†	49.0±24.0	19.6±9.7	68.8±33.6	27.6±13.8	42.9±21.3	16.8±8.7
Patient 8	47.4±21.1	22.4±12.0	112.1±47.4	52.5±28.0	68.6±29.7	31.9±17.6
Patient 9	66.7±31.4	24.1±13.0	117.4±53.9	42.7±23.1	67.4±29.7	24.3±17.6
Patient 10	41.4±19.3	16.8±8.3	131.8±55.6	53.18±26.3	84.7±32.7	33.8±13.3
Average*	51.5±7.8	24.0±3.9	110.0±28.3	44.2±13.9	72.5±17.2	28.4±7.4

Note: Data are reported as mean ± standard deviation.
*Patient 6 was excluded when deriving the average over the group, as a large ringing artefact was observed.
†Patient received radiation therapy.

for WM. One should note that a wide range of perfusion values can be found in literature. Therefore, we should be cautious not to overinterpret these numbers. However, the CBF values obtained when using DCE–AIFs seem to be more in line with literature values. Clearly, only a comparison with a true gold standard measured simultaneously would be conclusive.

The rCBV is a biomarker that is often applied clinically to characterize brain tumors and to monitor treatment response.[53–57] Since it is calculated as the ratio between the area under the tissue concentration curve and the integral under the curve of the first bolus passage of the AIF, it is directly affected by the choice for a particular AIF. Essentially, the area under the first contrast passage acts as a scaling factor of the CBV. This also implies that when calculating the ratio of CBVs from a tumorous region and a collateral ROI, such effects will cancel out. CBF values can, however, be more nonlinearly dependent on the shape of the AIF. Statistics on the area under the first passage of our AIFs is included in the supplementary material. This confirms the larger variation of the DSC–AIFs compared with the DCE–AIFs.

Our results may indicate that clinical research could be improved as follows. First, DCE imaging could enhance perfusion analysis from DSC MRI by providing a more reliable AIF. Such a DCE sequence can be acquired with minimal loss of imaging time, since the AIF can be measured during injection of the preload bolus. In our study, we employed a longer DCE sequence, since we also aim to improve leakage quantification by combining DCE and DSC analysis in our future work; this is, however, not necessary when the only goal is to measure the AIF. For that purpose the same scan duration as the DSC sequence could be chosen. Second, having a DCE–AIF in absolute concentration units could allow us to make CBV, CBF, and MTT measurements from DSC MRI more quantitative. Clearly, a remaining obstacle would be the lack of a suitable transformation, linear or nonlinear, to convert the DSC tissue signal into physical contrast concentration units. When the relaxivities of different tissue types such as GM, WM, tumor, and necrotic tissue can be estimated, however, then an accurate aCBF map in every individual can be generated.

There are several limitations of our study. First, the employed echo time (45 ms) is longer than currently advised (i.e., 25–35 ms).[58] Moreover, we did not have a ground-truth AIF in our study, as this can only be obtained by arterial blood sampling. Also, a ground-truth CBF was not available for similar reasons. In addition, the aCBF was derived with a particular R_2^* value for tissue and blood (to convert the DSC signal to contrast-agent concentration). While the R_2^* in both tissue and blood is still under debate, clearly our results will vary, with different R_2^* values for tissue or blood. Finally, the injection dose was not adjusted according to patient weight, but fixed at 7.5 ml for all patients. This bias was corrected by using an AIF model with normalized area under the bolus peak.

5 | CONCLUSION

We conclude that DCE-based AIFs are obtained efficiently during preload contrast-agent injection prior to DSC imaging. DCE-based AIFs are reproduced better across vessels than DSC-based AIFs, and can therefore improve the reliability of assessing perfusion parameters from

DSC MRI. In addition, the quantitative nature of DCE–AIFs demonstrates great potential for quantifying perfusion parameter estimates from DSC MRI truly.

ACKNOWLEDGEMENTS

We thank HollandPTC–Varian Consortium and Medical Delta Cancer Diagnostics 3.0 for supporting our project financially.

CONFLICT OF INTEREST STATEMENT

Author Marion Smits is a paid consultant of Bracco and receives speaker fees from AuntMinnie and GE Healthcare. No other conflict of interest was reported from other authors.

DATA AVAILABILITY STATEMENT

The data that support the findings of this study are available on request from the corresponding author. The data are not publicly available due to privacy or ethical restrictions.

ORCID

Chih-Hsien Tseng https://orcid.org/0000-0001-8692-6047

Matthias J.P. van Osch https://orcid.org/0000-0001-7034-8959

REFERENCES

1. Østergaard L, Weisskoff RM, Chesler DA, Gyldensted C, Rosen BR. High resolution measurement of cerebral blood flow using intravascular tracer bolus passages. Part I: Mathematical approach and statistical analysis. *Magn Reson Med*. 1996;36(5):715-725.
2. Calamante F. Perfusion MRI using dynamic-susceptibility contrast MRI: quantification issues in patient studies. *Top Magn Reson Imaging: TMRI*. 2010; 21(2):75-85.
3. Huang A, Lee C-W, Liu H-M. Time to peak and full width at half maximum in MR perfusion: valuable indicators for monitoring moyamoya patients after revascularization. *Sci Rep*. 2021;11(1):479.
4. Zierler K. Indicator dilution methods for measuring blood flow, volume, and other properties of biological systems: A brief history and memoir. *Ann Biomed Eng*. 2000;28(8):836-848.
5. Van Osch MJP, Vonken E-PA, Viergever MA, van der Grond J, Bakker CJG. Measuring the arterial input function with gradient echo sequences. *Magn Reson Med*. 2003;49(6):1067-1076.
6. Akbudak E, Kotys M, Conturo T. Quadraticity and haematocrit dependence of ΔR2* AIF signals at 3T: A blood phantom study under physiologic conditions. In: Syllabus of the ISMRM Workshop on Quantitative Cerebral Perfusion Imaging Using MRI; A Technical Perspective; Oral session 1. Venice, Italy; 2004.
7. Kjølby BF, Østergaard L, Kiselev VG. Theoretical model of intravascular paramagnetic tracers effect on tissue relaxation. *Magn Reson Med*. 2006;56(1): 187-197.
8. Van Dorth D, Venugopal K, Poot DHJ, et al. Dependency of R2 and R2* relaxation on Gd-DTPA concentration in arterial blood: Influence of hematocrit and magnetic field strength. *NMR Biomed*. 2022;35(5):e4653.
9. van Osch MJP, Vonken E-PA, Bakker CJG, Viergever MA. Correcting partial volume artifacts of the arterial input function in quantitative cerebral perfusion MRI. *Magn Reson Med*. 2001;45(3):477-485.
10. Ebinger M, Brunecker P, Jungehülsing GJ, et al. Reliable perfusion maps in stroke MRI using arterial input functions derived from distal middle cerebral artery branches. *Stroke*. 2010;41(1):95-101.
11. Rausch M, Scheffler K, Rudin M, Radü EW. Analysis of input functions from different arterial branches with gamma variate functions and cluster analysis for quantitative blood volume measurements. *Magn Reson Imaging*. 2000;18(10):1235-1243.
12. Shen Y, Goerner FL, Snyder C, et al. T1 relaxivities of gadolinium-based magnetic resonance contrast agents in human whole blood at 1.5, 3, and 7 T. *Investigative Radiol*. 2015;50(5):330-338.
13. Roberts C, Little R, Watson Y, Zhao S, Buckley DL, Parker GJM. The effect of blood inflow and B(1)-field inhomogeneity on measurement of the arterial input function in axial 3D spoiled gradient echo dynamic contrast-enhanced MRI. *Magn Reson Med*. 2011;65(1):108-119.
14. Garpebring A, Wirestam R, Ostlund N, Karlsson M. Effects of inflow and radiofrequency spoiling on the arterial input function in dynamic contrast-enhanced MRI: A combined phantom and simulation study. *Magn Reson Med*. 2011;65(6):1670-1679.
15. Wang H, Cao Y. Correction of arterial input function in dynamic contrast-enhanced MRI of the liver. *J Magn Reson Imaging: JMRI*. 2012;36(2):411-421.
16. Murase K. Efficient method for calculating kinetic parameters using T1-weighted dynamic contrast-enhanced magnetic resonance imaging. *Magn Reson Med*. 2004;51(4):858-862.
17. Van Schie JJN, Lavini C, van Vliet LJ, Vos FM. Estimating the arterial input function from dynamic contrast-enhanced MRI data with compensation for flow enhancement (I): Theory, method, and phantom experiments. *J Magn Reson Imaging*. 2018;47(5):1190-1196.
18. De Bazelaire C, Rofsky NM, Duhamel G, et al. Combined T2* and T1 measurements for improved perfusion and permeability studies in high field using dynamic contrast enhancement. *Eur Radiol*. 2006;16(9):2083-2091.
19. Quarles CC, Gochberg DF, Gore JC, Yankeelov TE. A theoretical framework to model DSC-MRI data acquired in the presence of contrast agent extravasation. *Phys Med Biol*. 2009;54(19):5749-5766.
20. Boxerman JL, Prah DE, Paulson ES, Machan JT, Bedekar D, Schmainda KM. The Role of Preload and Leakage Correction in Gadolinium-Based Cerebral Blood Volume Estimation Determined by Comparison with MION as a Criterion Standard. *Am J Neuroradiol*. 2012;33(6):1081-1087.

21. Saranathan M, Rettmann DW, Hargreaves BA, Clarke SE, Vasanawala SS. DIfferential subsampling with cartesian ordering (DISCO): A high spatio-temporal resolution dixon imaging sequence for multiphasic contrast enhanced abdominal imaging. *J Magn Reson Imaging*. 2012;35(6):1484-1492.
22. Friston KJ, Holmes AP, Worsley KJ, Poline J-P, Frith CD, Frackowiak RSJ. Statistical parametric maps in functional imaging: A general linear approach. *Hum Brain Mapp*. 1994;2(4):189-210.
23. Peruzzo D, Bertoldo A, Zanderigo F, Cobelli C. Automatic selection of arterial input function on dynamic contrast-enhanced MR images. *Comput Methods Prog Biomed*. 2011;104(3):e148-e157.
24. Orton MR, d'Arcy JA, Walker-Samuel S, et al. Computationally efficient vascular input function models for quantitative kinetic modelling using DCE-MRI. *Phys Med Biol*. 2008;53(5):1225-1239.
25. Wake N, Chandarana H, Rusinek H, et al. Accuracy and precision of quantitative DCE-MRI parameters: How should one estimate contrast concentration? *Magn Reson Imaging*. 2018;52:16-23.
26. Zhang X, Petersen ET, Ghariq E, et al. In vivo blood T1 measurements at 1.5 T, 3 T, and 7 T. *Magn Reson Med*. 2013;70(4):1082-1086.
27. Østergaard L, Sorensen AG, Kwong KK, Weisskoff RM, Gyldensted C, Rosen BR. High resolution measurement of cerebral blood flow using intravascular tracer bolus passages. Part II: Experimental comparison and preliminary results. *Magn Reson Med*. 1996;36(5):726-736.
28. Rempp KA, Brix G, Wenz F, Becker CR, Gückel F, Lorenz WJ. Quantification of regional cerebral blood flow and volume with dynamic susceptibility contrast-enhanced MR imaging. *Radiology*. 1994;193(3):637-641.
29. Wu O, Østergaard L, Weisskoff RM, Benner T, Rosen BR, Sorensen AG. Tracer arrival timing-insensitive technique for estimating flow in MR perfusion-weighted imaging using singular value decomposition with a block-circulant deconvolution matrix. *Magn Reson Med*. 2003;50(1):164-174.
30. Lind E, Knutsson L, Kämpe R, Ståhlberg F, Wirestam R. Assessment of MRI contrast-agent concentration by quantitative susceptibility mapping (QSM): Application to estimation of cerebral blood volume during steady state. *Magma (New York, NY)*. 2017;30(6):555-566.
31. Kellner E, Mader I, Mix M, et al. Arterial input function measurements for bolus tracking perfusion imaging in the brain. *Magn Reson Med*. 2013;69(3):771-780.
32. Kellner E, Mader I, Reisert M, Urbach H, Kiselev VG. Arterial input function in a dedicated slice for cerebral perfusion measurements in humans. *Magma (New York, NY)*. 2018;31(3):439-448.
33. Knutsson L, Lindgren E, Ahlgren A, et al. Dynamic susceptibility contrast MRI with a prebolus contrast agent administration design for improved absolute quantification of perfusion. *Magn Reson Med*. 2014;72(4):996-1006.
34. Calamante F. Arterial input function in perfusion MRI: A comprehensive review. *Prog Nucl Magn Reson Spectrosc*. 2013;74:1-32.
35. Murase K, Kikuchi K, Miki H, Shimizu T, Ikezoe J. Determination of arterial input function using fuzzy clustering for quantification of cerebral blood flow with dynamic susceptibility contrast-enhanced MR imaging. *J Magn Reson Imaging: JMRI*. 2001;13(5):797-806.
36. Carroll TJ, Rowley HA, Haughton VM. Automatic Calculation of the Arterial Input Function for Cerebral Perfusion Imaging with MR Imaging. *Radiology*. 2003;227(2):593-600.
37. Mouridsen K, Christensen S, Gyldensted L, Østergaard L. Automatic selection of arterial input function using cluster analysis. *Magn Reson Med*. 2006;55(3):524-531.
38. You S-H, Choi SH, Kim TM, et al. Differentiation of High-Grade from Low-Grade Astrocytoma: Improvement in Diagnostic Accuracy and Reliability of Pharmacokinetic Parameters from DCE MR Imaging by Using Arterial Input Functions Obtained from DSC MR Imaging. *Radiology*. 2018;286(3):981-991.
39. Kang KM, Choi SH, Chul-Kee P, et al. Differentiation between glioblastoma and primary CNS lymphoma: application of DCE-MRI parameters based on arterial input function obtained from DSC-MRI. *Eur Radiol*. 2021;31(12):9098-9109.
40. Lim WH, Park JS, Park J, Choi SH. Assessing the reproducibility of high temporal and spatial resolution dynamic contrast-enhanced magnetic resonance imaging in patients with gliomas. *Sci Rep*. 2021;11(1):23217.
41. Calamante F, Vonken E-PA, van Osch MJP. Contrast agent concentration measurements affecting quantification of bolus-tracking perfusion MRI. *Magn Reson Med*. 2007;58(3):544-553.
42. Pedersen M, Klarhöfer M, Christensen S, et al. Quantitative cerebral perfusion using the PRESTO acquisition scheme. *J Magn Reson Imaging*. 2004;20(6):930-940.
43. Lind E, Knutsson L, Ståhlberg F, Wirestam R. Dynamic contrast-enhanced QSM for perfusion imaging: a systematic comparison of Δ R2*- and QSM-based contrast agent concentration time curves in blood and tissue. *MAGMA*. 2020;33(5):663-676.
44. Knutsson L, Ståhlberg F, Wirestam R, van Osch MJP. Effects of blood Δ R2* nonlinearity on absolute perfusion quantification using DSC-MRI: Comparison with Xe-133 SPECT. *Magn Reson Imaging*. 2013;31(5):651-655.
45. Carroll TJ, Horowitz S, Shin W, et al. Quantification of cerebral perfusion using the "bookend technique": An evaluation in CNS tumors. *Magn Reson Imaging*. 2008;26(10):1352-1359.
46. Günther M, Bock M, Schad LR. Arterial spin labeling in combination with a look-locker sampling strategy: Inflow turbo-sampling EPI-FAIR (ITS-FAIR). *Magn Reson Med*. 2001;46(5):974-984.
47. Shin W, Horowitz S, Ragin A, Chen Y, Walker M, Carroll TJ. Quantitative cerebral perfusion using dynamic susceptibility contrast MRI: Evaluation of reproducibility and age- and gender-dependence with fully automatic image postprocessing algorithm. *Magn Reson Med*. 2007;58(6):1232-1241.
48. Petersen ET, Mouridsen K, Golay X, all named co-authors of the QUASAR test-retest study. The QUASAR reproducibility study, Part II: Results from a multi-center Arterial Spin Labeling test-retest study. *NeuroImage*. 2010;49(1):104-113.
49. Okazawa H, Yamauchi H, Sugimoto K, et al. Quantitative Comparison of the Bolus and Steady-State Methods for Measurement of Cerebral Perfusion and Oxygen Metabolism: Positron Emission Tomography Study Using 15O-Gas and Water. *J Cereb Blood Flow Metab*. 2001;21(7):793-803.
50. Leenders KL, Perani D, Lammertsma AA, et al. Cerebral blood flow, blood volume and oxygen utilization. *Brain*. 1990;113(1):27-47.
51. Ito H, Kanno I, Kato C, et al. Database of normal human cerebral blood flow, cerebral blood volume, cerebral oxygen extraction fraction and cerebral metabolic rate of oxygen measured by positron emission tomography with 15O-labelled carbon dioxide or water, carbon monoxide and oxygen: A multicentre study in Japan. *Eur J Nucl Med Mol Imaging*. 2004;31(5):635-643.
52. Rostrup E, Law I, Pott F, Ide K, Knudsen GM. Cerebral hemodynamics measured with simultaneous PET and near-infrared spectroscopy in humans. *Brain Res*. 2002;954(2):183-193.

53. Law M, Oh S, Babb JS, et al. Low-grade gliomas: Dynamic susceptibility-weighted contrast-enhanced perfusion MR imaging–prediction of patient clinical response. *Radiology*. 2006;238(2):658-667.
54. Kickingereder P, Wiestler B, Burth S, et al. Relative cerebral blood volume is a potential predictive imaging biomarker of bevacizumab efficacy in recurrent glioblastoma. *Neuro-oncology*. 2015;17(8):1139-1147.
55. Bell LC, Semmineh N, An H, et al. Evaluating the Use of rCBV as a Tumor Grade and Treatment Response Classifier Across NCI Quantitative Imaging Network Sites: Part II of the DSC-MRI Digital Reference Object (DRO) Challenge. *Tomography (Ann Arbor, Mich)*. 2020;6(2):203-208.
56. Schmainda KM, Zhang Z, Prah M, et al. Dynamic susceptibility contrast MRI measures of relative cerebral blood volume as a prognostic marker for overall survival in recurrent glioblastoma: Results from the ACRIN 6677/RTOG 0625 multicenter trial. *Neuro-oncology*. 2015;17(8):1148-1156.
57. Henriksen OM, Del Mar Álvarez-Torres M, Figueiredo P, et al. High-Grade Glioma Treatment Response Monitoring Biomarkers: A Position Statement on the Evidence Supporting the Use of Advanced MRI Techniques in the Clinic, and the Latest Bench-to-Bedside Developments. Part 1: Perfusion and Diffusion Techniques. *Front Oncol*. 2022;12:810263.
58. Boxerman JL, Quarles CC, Hu LS, et al. Consensus recommendations for a dynamic susceptibility contrast MRI protocol for use in high-grade gliomas. *Neuro-Oncology*. 2020;22(9):1262-1275.

SUPPORTING INFORMATION

Additional supporting information can be found online in the Supporting Information section at the end of this article.

How to cite this article: Tseng C-H, Jaspers J, Romero AM, et al. Improved reliability of perfusion estimation in dynamic susceptibility contrast MRI by using the arterial input function from dynamic contrast enhanced MRI. *NMR in Biomedicine*. 2023;e5038. doi:10.1002/nbm.5038